Microwave-Heating Induced Temperature Gradients in Liquid-Liquid Biphasic Systems

Tai-Ying Chen[1†], Montgomery Baker-Fales[1†], Himanshu Goyal[2], and Dionisios G. Vlachos[1,3,*]

[1]Department of Chemical and Biomolecular Engineering, University of Delaware, 150 Academy Street, Newark, Delaware 19716, United States

[2]Department of Chemical Engineering, Indian Institute of Technology Madras, Chennai, Tamil Nadu 600036, India

[3]Catalysis Center for Energy Innovation, RAPID Manufacturing Institute, and Delaware Energy Institute (DEI), 221 Academy St., University of Delaware, Newark, Delaware 19716, United States

†These authors contributed equally.

*Corresponding author: vlachos@udel.edu

Abstract

Microwaves (MWs) can enable the electrification and intensification of chemical manufacturing. They have been applied to various unit separations, such as drying, distillation, and extraction, entailing gas-liquid and solid-liquid systems. However, a limited quantitative understanding of MW-heated liquid-liquid biphasic systems related to extraction exists. This work measures the temporal and spatial temperature difference between an aqueous and an organic phase in batch and continuous microfluidic modes. We demonstrate permanent temperature differences between phases over 35 °C and spatiotemporal periodic and quasiperiodic oscillations modulated by the flow patterns. The temperature differences are primarily driven by the faster absorption rate of microwave irradiation by the aqueous phase vs. the slower heat transfer from the aqueous phase to the organic phase. These are amplified by low specific interfacial area and modifications of the electromagnetic field. We employ a multiphysics model to predict the temperature difference in a batch system. The model is in good agreement with the experiments. We demonstrate a strong effect of input power, dielectric properties of organic solvents, the volume of solvents, and the volume ratio between phases on the temperature difference. A simple analytical model describes the temperature difference and provides design principles. The combined approach offers new insights into the design and optimization of the MW-heated biphasic systems.

Keywords: Biphasic system, heat transfer, microfluidics, microwave heating, extraction

Introduction

Electromagnetic energy generated from renewable sources is an emerging route toward process intensification, electrification, and decarbonization of chemical manufacturing.[1–5] Electromagnetic radiation, such as microwaves (MWs), can heat rapidly, volumetrically, and selectively to overcome the heat transfer limitations of conventional processes.[6–12] Multiphase systems, especially those with disparate dielectric permittivity, are uniquely impacted by selective MW heating and can sustain distinct phase temperatures.[13–17] This effect can yield energy savings, enhanced separation efficiency, and higher reaction selectivity.[18–21] MW heating is applied to many separations, such as drying, extraction, and distillation.[22–27] These separations are mostly gas-liquid or solid-liquid systems. For instance, MW heating is widely used to extract antioxidants from vegetables, wastes, and plants.[28–32] MWs provide a higher recovery rate than conventional solvent extraction.[22] MW-assisted distillation has received attention as it significantly affects the polar components' vapor concentration and induces selective vaporization.[27,33] These MW-assisted separations underscore the potential of MWs for process intensification.

MW radiation has recently been applied to liquid-liquid extraction.[34–37] In a typical liquid-liquid extraction, water and a non-polar organic solvent are chosen as bulk liquids, and a target molecule (solute) is extracted from the aqueous to the organic phase. MW radiation typically heats the aqueous phase faster than the non-polar organic phase due to their respective dielectric properties, resulting in a sustained temperature gradient between the two liquids. This temperature gradient promotes extraction efficiency and improves product yield and selectivity.[34–37] For example, Ricciardi *et al.*[36] reported that for furfural production via reactive extraction, selectivity is enhanced by employing MW radiation and low-dielectric-constant organic solvents. Similarly, Breeden *et al.*[34] showed that in a water/dichloroethane biphasic system, 5-chloromethyl furfural selectivity is significantly improved.

An understanding of MW-heated liquid-liquid biphasic systems is currently lacking, which hinders the design of MW-assisted biphasic extractors and reactors. One significant barrier is the lack of measuring temperature in the aqueous and organic phases. To our knowledge, no work has directly and precisely measured the temperature of both phases to rationalize the advantage of selective heating. This dearth of foundational literature owes to the often-discussed complications of temperature measurements inherent to MW systems[36,38,39]: thermocouples are unsuited to the MW environment, and optical methods (pyrometer, thermal camera, etc.) only measure surface temperatures. Alternatively, temperature-sensing optical fibers can be immersed similarly to thermocouples, are well-suited to MW environments, and provide good spatial accuracy. However, liquid-liquid systems must be pressurized at reaction-relevant temperatures, e.g., >100 °C, making optical fiber usage more challenging, especially given their fragility. Furthermore, the fast-changing temperatures of MW-heated biphasic continuous flow systems add further complications. Simulations in MW literature often accompany experimental works[40–42]. There are a few studies on modeling and investigating the MW heating of the liquids[43–47]. For example, Ayappa *et al.*[43] investigated the natural convection in a square cavity numerically and found the location of power peaks would affect the temperature uniformity. Chatterjee *et al.*[44] investigated the effect of rotation and natural convection on MW heating of liquids and indicated that the former does not improve the temperature uniformity. Moreover, Rattanadecho *et al.*[45,47] modeled the microwave heating of

liquids using a rectangular waveguide and demonstrated the effect of the dielectric properties and the sample size. Although these works have advanced the understanding of the single-phase liquid medium under MW radiation, studies on liquid-liquid biphasic systems under MW radiation are still limited because of the multiphase and multiphysics nature of the problem.[17,48]

This work focuses on measuring and predicting the microwave heating of liquid-liquid biphasic systems. We precisely measure the temperature difference between two phases in batch and continuous flow modes. We establish a multiphysics model to predict the temperature difference in a batch system and compare the results to experiments. Then, we combine simulations and experiments to investigate the effect of various processing parameters on the temperature difference. Moreover, we develop an analytical model to describe the temperature of each phase in biphasic systems, rationalize the observed temperature difference, and provide guidelines for engineering the temperature difference.

Methods

Experimental Methods

Both batch and flow experiments are showcased in this work. Custom-built attenuator rigs were fabricated for use with a CEM Discover SP microwave applicator. The batch rig, shown in Scheme 1a, accommodates 10 mL borosilicate vials available from CEM. Temperature is measured simultaneously by two FISO FOT-L-SD fibers housed in parallel sapphire thermowells. One fiber is interrogated by the CEM reactor and used for temperature feedback, while the other is interrogated by a FISO UMI-4 Multichannel Instrument, independent of the control scheme. In a typical batch experiment, water and organic solvent are added to the vial having a stir bar; the vial is sealed into the attenuator and then pressurized with inert gas (helium; 15 bar) before heating to avoid an otherwise-observed violent boiling phase. Pressure has no little-to-no effect on the dielectric properties for solvents below their critical point; therefore, the effect of pressure is not explored.[6] At high stir (900 rpm), the vial is heated with either a controlled or constant power scheme. A mapping of the axial coordinate system for the batch rig – starting from the internal floor of the vial – is shown in Scheme 1a. The temperature is measured at various axial locations in the vial, yielding both the spatial and temporal temperatures in the biphasic system.

The flow rig, shown in Scheme 1b, is described in our previous work[49], and consists of a polytetrafluoroethylene (PTFE) insert affixed to the aluminum attenuator to guide tubing in a "U" shape through the microwave cavity. The microchannel is constructed from ethylene tetrafluoroethylene (ETFE) of various diameters, sourced from IDEX Health & Science LLC. Water and organic solvents are pumped independently from two Teledyne ReaXus LS-Class pumps, joined via a flow tee (IDEX #P-713) into one channel, and then enter the cavity after a 50 cm single-channel flow to help ensure flow-regime stability. This channel ends at a custom flow tee, where an optical fiber is inserted directly into the flow path (counter to the flow direction), and sealed into the system using ETFE ferrules and a perfluoroalkoxy alkane (PFA) sheath. We utilize OpSens M360 fibers, made of silica-clad and silica-sealed to withstand direct pressure, elevated temperatures, and moderately aggressive solvents without being affected. The fibers can be fixed at any axial location in the microchannel. An OpSens CoreSens GSX-2 unit capable of

measurements at 1000 Hz is used for interrogation. In a typical flow experiment, the sealed system is subjected to 150 psi of backpressure, and total flowrates are set from 0.010 to 4.000 mL/min. The system applies constant power for 2-5 min, and temperatures are analyzed after the system reaches a steady state, typically between 1-2 min.

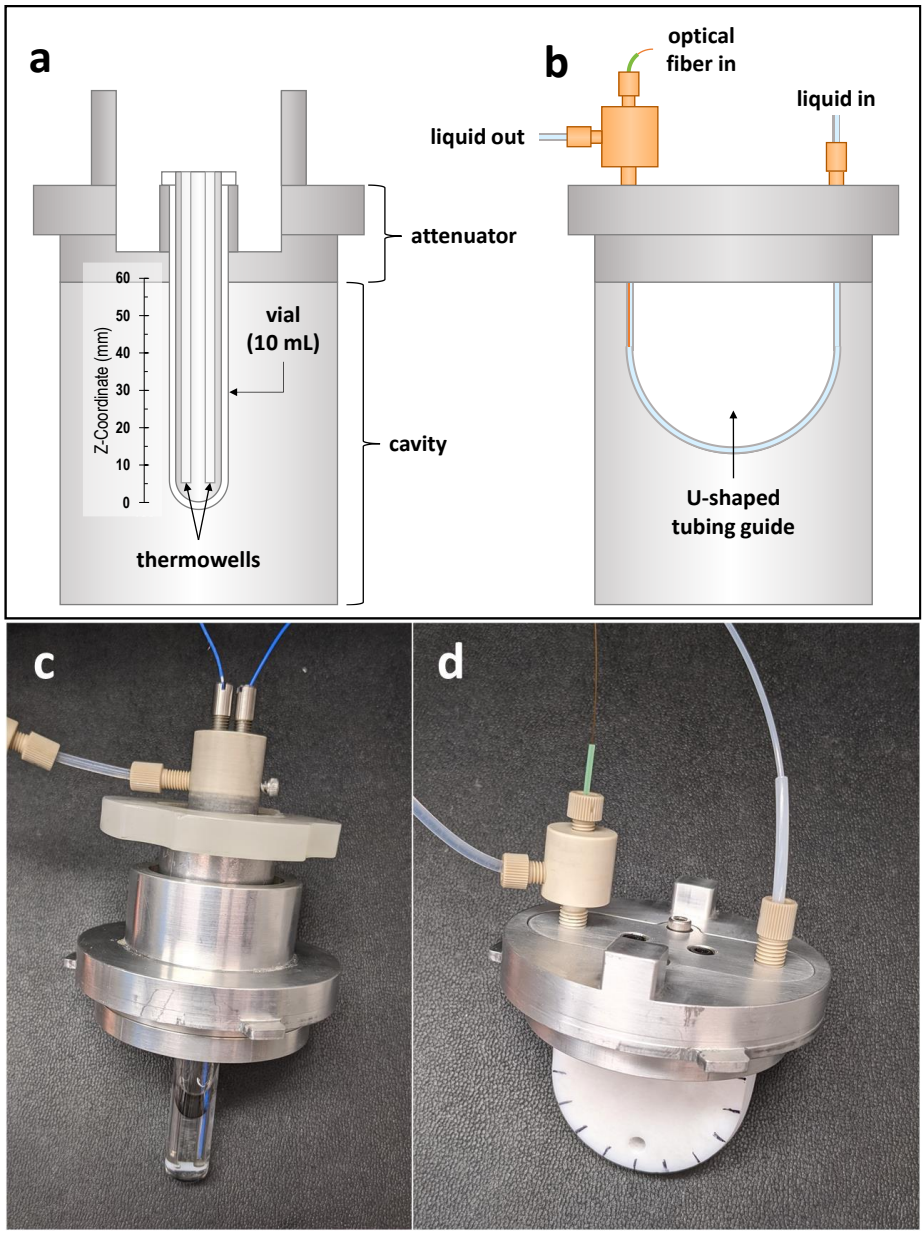

Scheme 1. Diagrams of batch (a) and flow (b) attenuator rigs for the CEM Discover SP microwave applicator. Photographs of batch (c) and flow (d) attenuator rigs.

Chemicals used include: ultrapure water (Milli-Q purified), 2-pentanol (Sigma-Aldrich P8017, 98% purity), hexanes (Fisher Chemical H302-4; >98.5% purity), toluene (Sigma-Aldrich 179418;

>99.5% purity), methyl isobutyl ketone (MIBK) (Sigma-Alrich 360511; >98.5% purity), methylcyclohexane (Sigma-Alrich M37889; 99% purity), 2-methyltetrahydrofuran (Sigma-Alrich 673277; >99% purity), and cyclohexanol (Sigma-Alrich 105899; 99% purity). Dielectric properties were analyzed between 1.5 and 2.6 GHz at a temperature of 20°C using an ITACA Microwave Dielectric Measurement Kit.

Computational Methods

We model a 10 mL glass vial containing water and organic solvent in the CEM Discover SP MW cavity. We solve the electromagnetics, fluid dynamics, and heat transfer equations. The electromagnetic field in the cavity is described with the Helmholtz representation of the Maxwell's equation[40,50,51],

$$\nabla^2 \boldsymbol{E} + \varepsilon_r (\frac{2\pi f}{c_0})^2 \boldsymbol{E} = 0 \quad (1)$$

where $\boldsymbol{E}$ is the electromagnetic field, ε_r is the permittivity relative to that of vacuum, f represents the electromagnetic frequency; and c_0 denotes the speed of light in a vacuum. The permittivity is a complex number, composed by a (real) dielectric constant ε' and a (imaginary) loss factor ε''. The dielectric constant describes a material's polarizability, and the loss factor represents the ability of a material to dissipate electromagnetic energy into heat.[42] The ratio is termed the loss tangent $tan\delta = \varepsilon''/\varepsilon'$. The power dissipated into a medium, denoted as P_d, is described as[52],

$$P_d = \pi \varepsilon_0 \varepsilon" f |\boldsymbol{E}|^2 \quad (2)$$

where ε_0 is the dielectric permittivity of vacuum. This dissipated power serves as a heat generation term in the energy balance equation (Eq. 3).

$$\rho C_p \frac{\partial T}{\partial t} + \rho C_p \boldsymbol{U} \nabla T = -\nabla(\kappa \nabla T) + P_d \quad (3)$$

In Eq. 3, *T* denotes the temperature, ρ is the mass density, C_p is the specific heat capacity, $\boldsymbol{U}$ is the velocity, and κ is the thermal conductivity. To evaluate the spatial temperature field, the energy balance equation is solved together with Eq. 1, the continuity equation for incompressible fluids (Eq. 4), and the Navier-Stokes equation (Eq. 5).

$$\nabla \cdot \boldsymbol{U} = 0 \quad (4)$$

$$\frac{\partial(\rho \boldsymbol{U})}{\partial t} + \nabla \cdot (\rho \boldsymbol{U} \times \boldsymbol{U}) = \mu \nabla^2 \boldsymbol{U} - \nabla P + \rho \boldsymbol{g} \quad (5)$$

In Eq. 4, μ is the dynamic viscosity and P denotes the pressure. The aforementioned governing equations are implemented and solved using the COMSOL Multiphysics software, referenced hereafter as COMSOL. The RF module, the Heat Transfer module, and the Laminar Flow module are employed for time-dependent, three-dimensional simulations and solved using inbuilt finite element method solvers. The geometry of the CEM Discover SP cavity built in COMSOL is shown in Scheme 2 and is detailed in references[40,53]. The dimensions of the glass vial are the same as in the experiments. The metallic walls of the cavity are assumed as perfect conductors, making all

the electric and magnetic fields inside the conducting region zero. At the inlet, a traverse electric mode TE_{10} is applied. Heat loss due to natural convection is imposed at the outside of the vial. At the interface of two materials, thermal equilibrium is assumed, and the tangential components of the electric fields are continuous. The initial temperature is set at 20 °C. A zero-gradient for pressure and no-slip boundary condition for velocity are implemented at the wall of the vial. A mesh-dependency is performed to ensure that the results are independent of discretization. The mesh of the solvents is set to "Finer", of the glass vial wall to "Fine", and of the rest of the simulation domains to "Normal" in the *Physics-Controlled Mesh setting* in COMSOL. A typical number of mesh elements is around 10^6. Additional information can be found in the SI.

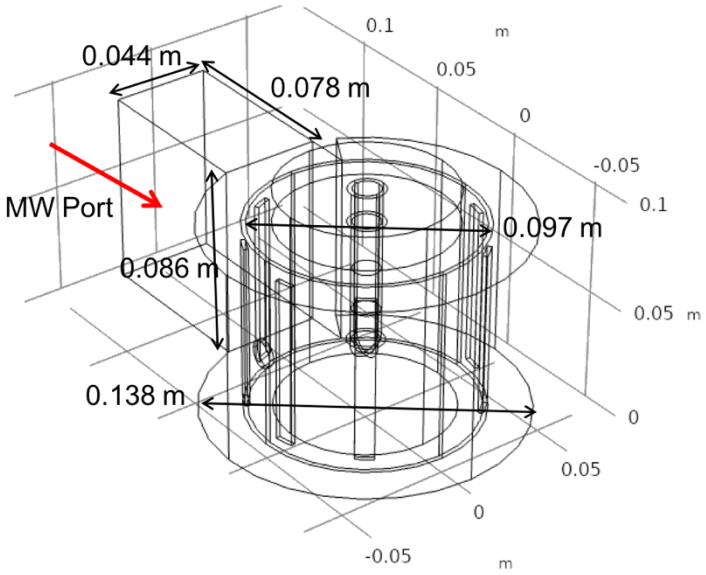

Scheme 2. Schematic of the CEM Discover SP MW applicator and the batch reactor modeled in COMSOL.

Results and Discussion

Temperature difference in the MW-heated batch system

When MW irradiation is applied to liquid-liquid biphasic systems, each phase is heated selectively and the temperatures can differ. This effect is illustrated in Figure 1, where both an aqueous system (6 mL water) and a biphasic system (3 mL water and 3 mL MIBK) are heated by microwaves. The input power is modulated to reach specified temperatures and maintained using the microwave applicator's control system. For both systems, a reference temperature (T_1) of 160 °C is measured and enforced at $z = 7.75\,mm$ from the bottom of the vial (because of the presence of a stir bar and the thermowell, this is incidentally the lowest possible temperature measurement location). A second fiber probes the temperature along the axial dimension. In the monophasic system (Figure 1a), the temperature is uniform in the axial dimension, cooling slightly near the liquid-gas boundary. In the biphasic system (Figure 1b), however, distinct temperature

regimes are observed: the temperature of the aqueous phase is maintained at the control temperature while the organic phase experiences a markedly lower temperature (~140 °C). This temperature difference is maintained at steady state using the control system and is hence referred to as ΔT_{ss}. In Figure 1c, the development of temperature and temperature difference with time in the same biphasic system is shown – this time with a static secondary fiber, located at the center of the organic phase ($z = 42.75\,mm$) and referred to as T_2. From the onset of heating, the temperature difference increases rapidly from zero, reaching a maximum (ΔT_{max}) in 1-2 min of irradiation and then gently descending to steady state. The existence of a persistent ΔT is attributed to the heating from the MW radiation being much faster than the heat transfer between the two phases, where the increase of T_2 mainly comes from the heat transfer from the aqueous to the organic phase. The transient ΔT_{max} is attributed to a combination of developing temperature gradients, modulating applied power (especially in the case of controlled systems), and temperature-dependent dielectric properties. For this particular system and experimental conditions, $\Delta T_{max} = 33.7 \pm 0.6\,℃$ and $\Delta T_{ss} = 20.2 \pm 0.3\,℃$ are observed across repeated experiments.

To control the ΔT_{ss}, a series of controlled-power experiments are performed to maintain T_1 at specified temperatures ranging from 60 to 200 °C. In Figure 1d, the ΔT increases when the control temperature increases. This is attributed to the rise in input power when the control temperature increases, where more energy is selectively dissipated into the water, leading to larger ΔT_{ss}. The relation between power and ΔT_{ss} seemingly changes as the temperature increases. At higher applied powers, larger increments in additional power are required to increase ΔT_{ss} by a given amount. This is attributed to the temperature dependence of dielectric properties, whereby lesser fractions of the applied power are likely to be absorbed at increasing temperatures. We then utilize COMSOL, discussed below, to further understand the temperature gradient and elucidate the effects of various parameters.

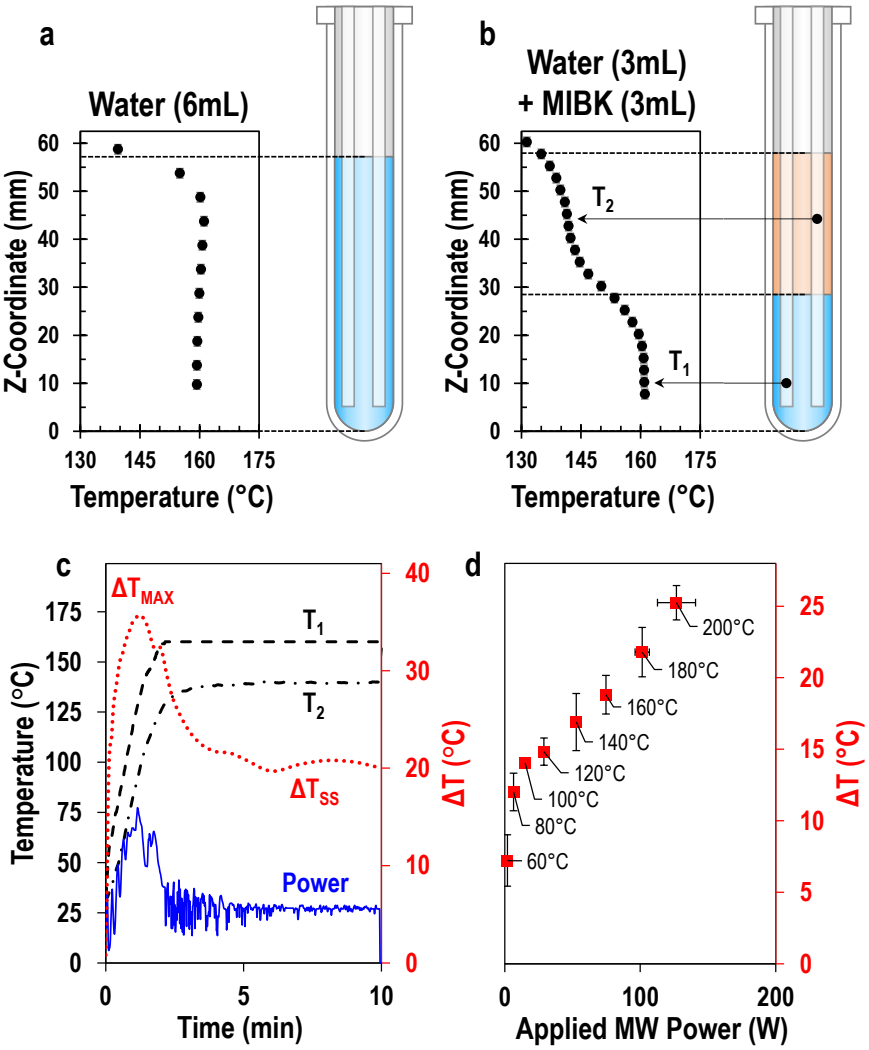

Figure 1. Experimental steady-state axial temperature profiles in a MW-heated aqueous system (a) and a biphasic system (b). Temperature development with time of MW-heated biphasic system (c). Effect of MW power (not to scale) on steady-state ΔT with aqueous phase temperatures denoted (d). Error bars for axial temperature data represent uncertainty in position (estimated to be 1.0 mm) and variance in the temperature over time of measurement (1 minute at each location). Error bars for ΔT data represent variance in average applied power and average ΔT over the steady portion of the batch heating experiment, all performed in triplicate.

CFD modeling of the microwave-heated batch system

COMSOL simulations of both single-phase batch and continuous flow reactors have been previously shown to predict the heating reasonably under microwave radiation.[40–42,49,53,54] The simulations here follow the experimental setup closely. We employ the transient experimental input power corrected with the previously reported calibration curve without alterations.[41] The dielectric

properties of MIBK are listed in Table 1 and of water in the SI. The time-dependent, transient temperature profiles of the aqueous phase for five temperatures (80 to 160 °C) in the biphasic system agree well with experiments (Figure S2). Figure 2a shows a clear temperature difference between the two phases, reminiscent of the experiments. This temperature difference is attributed to the direct MW heating of the aqueous phase and the heat transfer between phases, where both conduction and thermal gradient-induced Rayleigh convection contribute. The electric field (Figure 2b) is orders of magnitude higher at the bottom of the vial (in the aqueous phase) than at the top (in the organic phase). Interestingly, a strong electric field forms at all interfaces, i.e., between the aqueous and organic phases, the organic phase and air, and the solvents and the vial wall. The amplification of the electric field at the liquid-liquid interface is due to the sharp variation in the dielectric properties of different materials that concentrates the electric field. The electromagnetic energy is mainly dissipated into the aqueous phase, while barely any power goes into the organic phase. With an initial input power of 80 W, the absorbed power of the aqueous phase is ~39 W, while that of the organic phase is ~4 W (Figure 2c). In contrast, the temperature profile of a monophasic water system (Figure 2d) is much more uniform, consistent with the experiments. This temperature profile is more uniform than previously reported work[40], attributed to the enhanced mixing provided by the magnetic stirrer. Unlike the biphasic system, the electromagnetic energy is dissipated into the whole monophasic system (Figure 2e and f). This clearly explains the observed temperature difference between the two phases and demonstrates the selective nature of microwave heating. Such phenomena are caused by the different dielectric properties of solvents, where the energy dissipates into the high dielectric-loss materials. To further illustrate this point, below, we investigate the temperature difference using other organic solvents of varying dielectric properties.

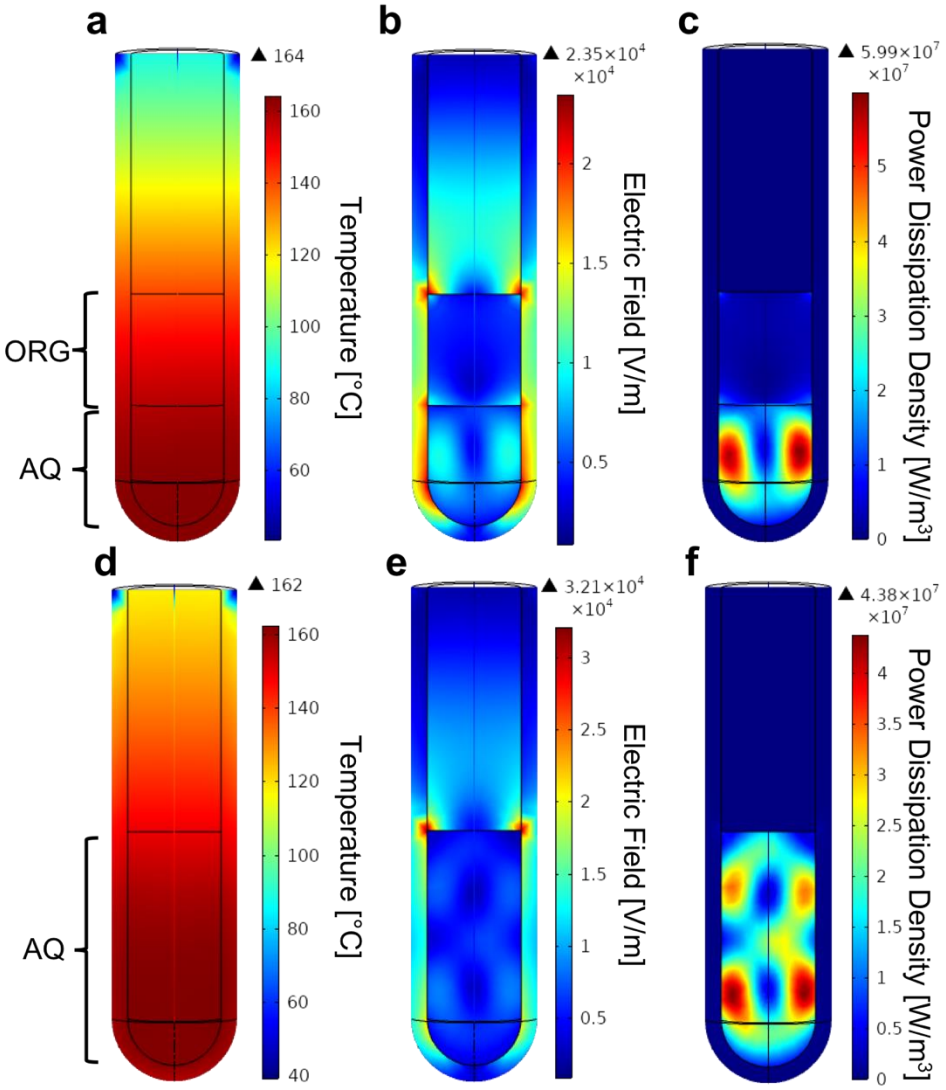

Figure 2. Temperature (a), electric field (b), and power density dissipation (c) profile of 1.5 mL water (bottom) and 1.5 mL MIBK (top) in a 10 mL vial; and temperature (d), electric field (e), and power density dissipation (f) of 3 mL water in a 10 mL vial at 160 °C.

Effect of the organic solvents and dielectric properties on the temperature difference

To understand the effect of dielectric properties on ΔT_{ss}, we screen a wide range of dielectric constants and loss tangents using COMSOL simulations. As shown in Figure 3a, ΔT_{ss} increases when the loss tangent decreases, indicating that a low loss tangent organic solvent achieves large ΔT_{ss} due to its inability to dissipate electromagnetic energy into heat. On the other hand, when the dielectric constant of organic phase increases, the ΔT_{ss} decreases. This is attributed to the ability of organic phase to absorb electromagnetic energy at high dielectric constant. It is noted that the

effect of the organic phase dielectric constant is less significant at low loss tangent, showing that ΔT_{ss} is a much stronger function of loss tangent than the dielectric constant. Figure 3b shows the power dissipation difference between two phases at 20 °C. A similar trend of power dissipation difference as in ΔT_{ss} clearly shows that the dielectric properties greatly affect the electromagnetic field in the cavity, and thus, the dissipated heat into each phase and the ΔT_{ss}.

In concert with the simulations, seven organic solvents were tested experimentally: 2-pentanol (2-pentOH), methyl isobutyl ketone (MIBK), 2-methyl tetrahydrofuran (2-mTHF), cyclohexanol, toluene, hexane, and m-cyclohexane. Their dielectric properties, measured at 20 °C, are shown in Table 1. These dielectric properties are at equilibrated conditions, where a small amount of the water is in the organic phase because of the mutual solubility. At a 1-to-1 ratio with water and a total volume of 6 mL, each system was heated such that the aqueous phase reached a steady-state temperature of 160 °C. Figure 3c shows that the ΔT_{ss} increases when the aqueous-to-organic loss tangent ratio increases. The m-cyclohexane, with the smallest low loss tangent ($tan\delta = 0.01$), shows the largest ΔT_{ss}, while the cyclohexanol, having a high loss tangent ($tan\delta = 0.47$), gives the smallest ΔT_{ss}. Some variation of individual solvents from the general trend exists because the ΔT_{ss} is not only affected by the dielectric properties but also other factors, such as the heat transfer between phases. The dielectric properties usually change when temperature increases, potentially contributing to the variation observed. Moreover, these experimental measurements, superimposed in Figure 3a, show a strong correlation between the ΔT_{ss} and loss tangent consistent with the simulations. This indicates that dielectric properties of the biphasic system play a significant role in determining ΔT_{ss} in microwave-heated biphasic systems.

Table 1. Dielectric properties of various organic solvents measured at 20 °C after equilibration with water.

Organic solvents	Dielectric constant [-]	Loss factor [-]	Loss tangent [-]	Loss tangent ratio (Aq/Org) [-]
MIBK	13.62	1.92	0.14	0.68
2-pentOH	5.24	3.20	0.61	0.16
2-mTHF	8.36	0.71	0.08	1.77
Toluene	2.36	0.02	0.01	11.29
Hexane	1.88	0.00	0.00	36.23
Cyclohexanol	4.46	2.11	0.47	0.23
m-cyclohexane	2.01	0.01	0.00	34.84

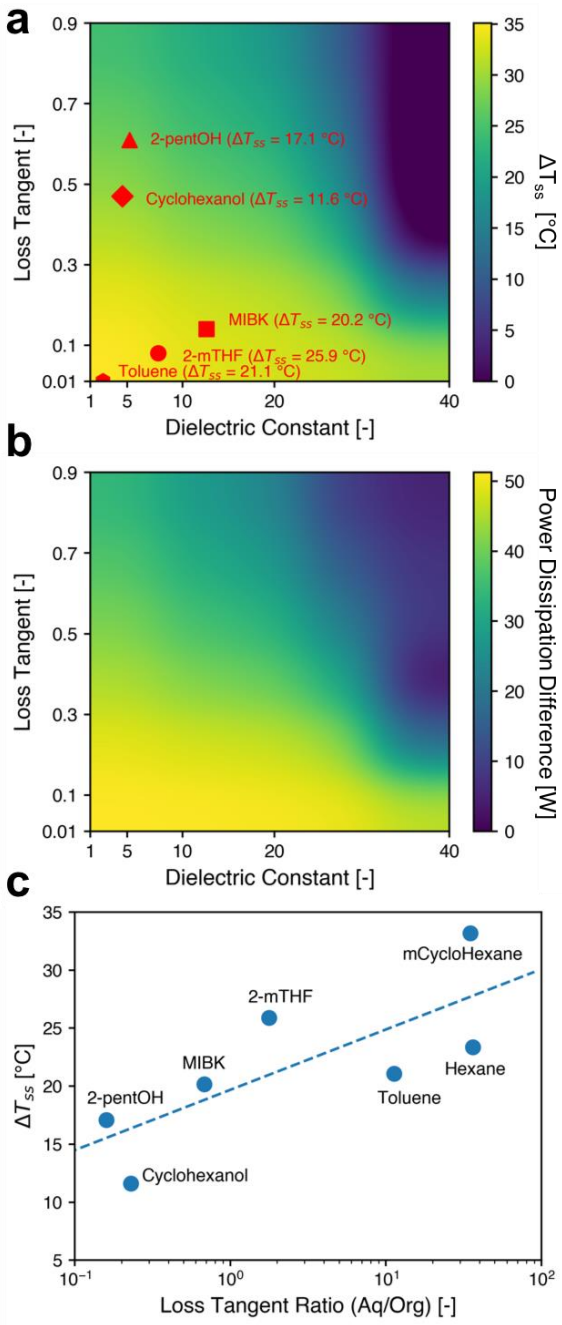

Figure 3. Predicted effect of dielectric constant and loss tangent of the organic solvents on ΔT_{ss} (a) and power dissipation difference (b). The points on the heatmap (a) represent the experimental measurements. Measured ΔT_{ss} for various aqueous-to-organic loss tangent ratios (c). The dashed line is a guide to the eyes. The conditions used are those of Figure 1c for different organic solvents.

Effect of solvent volumes and volume ratios

Dielectric properties aside, the volume of solvents and the volume ratio of the phases strongly affect ΔT_{ss}. Here we vary them in select experiments, keeping the total volume between 3 and 6 mL and the aqueous phase temperature at 160 °C. Since the volume of each phase and the interface location change, the water temperature is measured at the lowest possible location ($z = 7.75\ mm$), with the second fiber placed at the center of the organic phase. ΔT_{ss} (Figure 4) is taken after 10 minutes of controlled heating, at which steady-state is assumed. As the organic volume (V_{ORG}) increases along the constant aqueous volume (V_{AQ}) contours, enhancement of ΔT_{ss} is observed in most cases due to the more extensive energy requirements to increase the temperature of the organic phase. Similarly, as V_{AQ} increases along the constant-V_{ORG} contours, ΔT_{ss} enhancement is again observed due to a decrease in the specific surface area of the aqueous phase as its volume increases (given the geometry of the vial, the surface area is constant). For a fixed phase ratio (φ), as the total system volume increases, ΔT_{ss} increases monotonically. This is unsurprising, as larger organic phase volumes and smaller specific surface areas incur. Interestingly, as the phase ratio increases at constant system volume (i.e., 6 mL), ΔT_{ss} increases to a maximum (around φ = 2) and then decreases due to the competitive nature of the specific surface area and phase ratio.

In summary, changing the volume or volume ratio affects not only the heat transfer but also the electric field and power dissipation, which depend strongly on the load and geometry. The aqueous volume and volume ratio can be tuned to engineer a desired ΔT_{ss}. Moreover, these parameters significantly affect flow patterns in continuous flow systems. To elucidate this behavior, the temperature difference in our microfluidic system is investigated next.

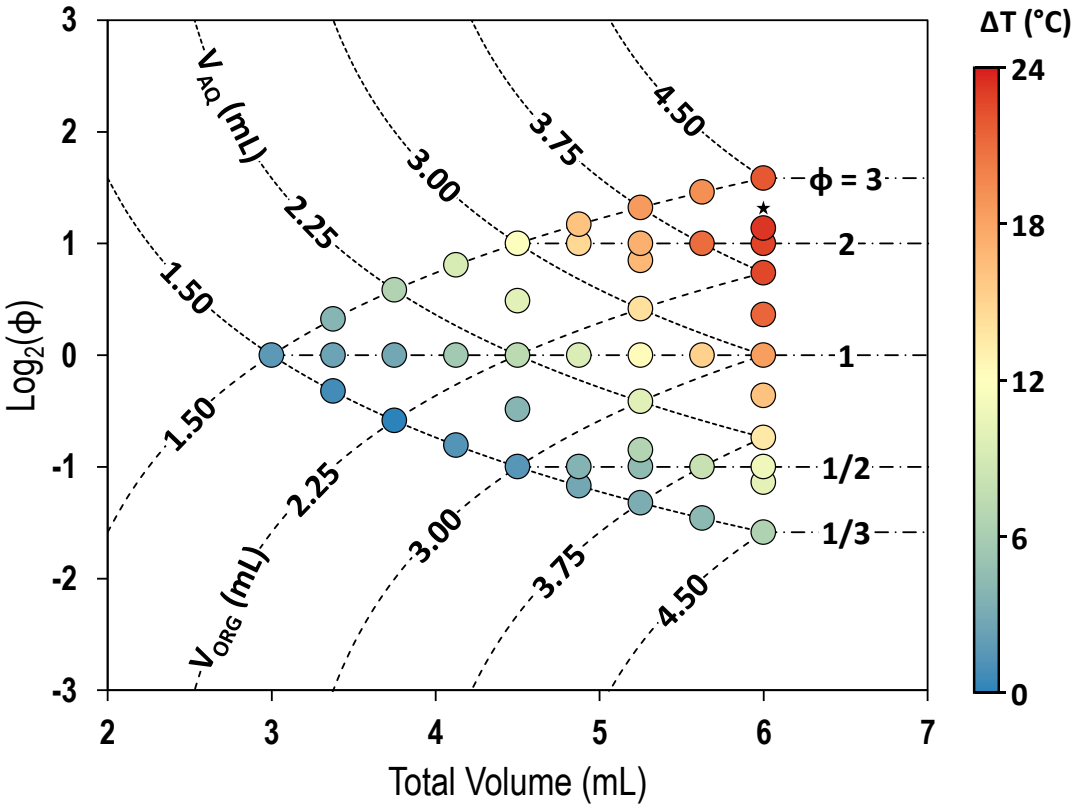

Figure 4. Measured ΔT_{ss} between phases for various volumes and volume ratios in batch systems. Temperature is denoted with color as shown in the scale. The ordinate axis is scaled to the logarithm of the phase ratio ($\varphi = V_{AQ}/V_{ORG}$) for equal distribution of similarly-scaled conditions. Contour lines for constant aqueous volumes, organic volumes, and phase ratios aid interpretation. A single star is placed above the global ΔT_{ss} maximum.

Temperature difference in MW-heated continuous micro- and milli-fluidic systems

To explore the effects of microwave irradiation on biphasic flow systems, a "U-shaped" microchannel described in previous work was employed.[49] ETFE tubing of an inner diameter of 0.030", 0.040", 0.063", and 0.093" is used to alter the specific surface area of biphasic flow. These diameters are in the micro- to milli-scale that, for simplicity, we refer to as microchannels. Such changes in diameter also provoke changes in the biphasic flow by altering the inertial, viscous, and surface forces.[55–58] For the water/MIBK system, specifically, in 0.030" and 0.040" ID tubing, slug-slug flow is observed at most flow rates studied (Figure 5a), while in the 0.063" and 0.093" ID tubing, a slightly more disordered slug-drop flow regime occurs at most flow rates (Figure 5d). In all cases, only segmented flow is observed. By mounting an optical fiber at a static location inside an MW-heated microchannel, we observe temperature periodic oscillations corresponding to aqueous and organic slugs. In analyzing this data, the oscillatory amplitude is inferred to be the ΔT between adjacent slugs (or drops), while the period corresponds to the length of each slug by multiplication with the superficial velocity. As shown in Figure 5b, the slug-slug flow regime

produces very neat, nearly sinusoidal oscillatory behavior. Conversely, shown in Figure 5e, the slug-drop flow regime produces a distribution of amplitudes and peak widths (less periodic data). This varied oscillatory behavior, owing to the various slug and drop sizes, directly influences the ΔT in Figure 5f, as peak amplitude and width are highly correlated. For the more periodic slug-slug flow regime (Figure 5c), much smaller distributions in amplitude and peak width are observed, with no clear correlation between ΔT and slug size. This can be attributed to the smaller distribution of slug sizes, where the effect of slug length on the ΔT is not as pronounced as in Figure 5f.

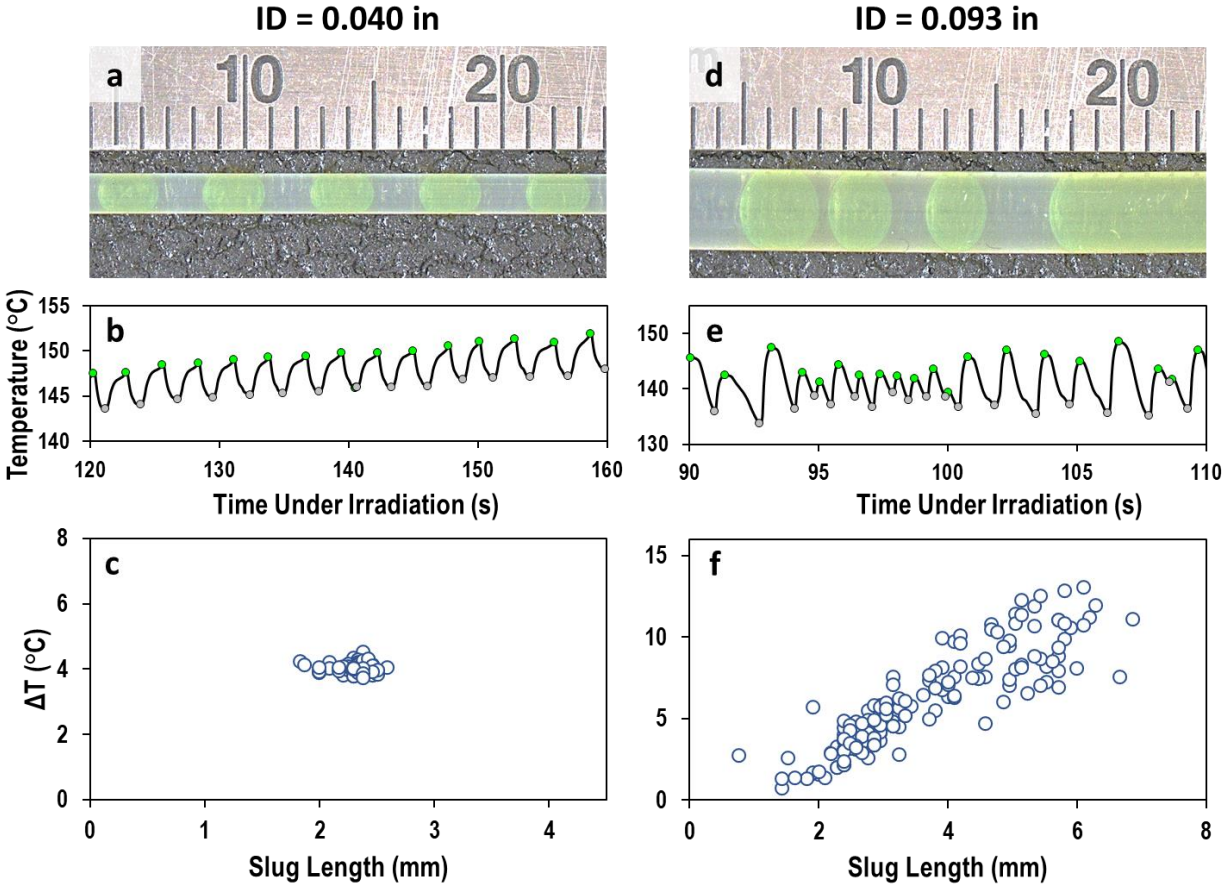

Figure 5. Temperature difference in MW-heated biphasic flow systems. Photographs of slug-slug and slug-drop flow regimes in 0.040" (a) and 0.093" (d) inner diameter tubes, respectively. Scale is in millimeters, and the aqueous phase is dyed yellow-green using sodium fluorescein. Oscillatory temperature in MW-heated slug-slug (b) and slug-drop (e) flow patterns – dye absent. Distribution of ΔT and slug size, as inferred from peak width, of the above slug-slug (c) and slug-drop (f) temperature profiles. Experiments in 0.040" tubing (a, b, and c) were performed at a 1:1 flowrate ratio and a total flow rate of 0.165 mL/min; experiments in 0.093" tubing (d, e, and f) were performed at a 1:1 flowrate ratio and a total flow rate of 4.000 mL/min.

By moving the temperature-sensing optical fiber throughout the length of the flow path, the axial temperature and ΔT_{ss} profiles can be mapped. Such a mapping is shown in Figure 6a after the system had come to steady-state (after 60 seconds of MW irradiation in 0.063" ID tubing with a 1:1 flow rate ratio and a total flow rate of 1.000 mL/min). In Figure 6a, black-filled circles indicate temperature averages for 60 seconds. Similarly, red squares indicate ΔT_{ss} averaged over the same period, with the full distribution shown as rose circles in the background. As the fluid enters the cavity, it heats in an accelerating fashion, reaches a peak temperature, and then loses heat after leaving the MW focal point, consistent with our previous work on pure water systems in the same microchannels.[49] ΔT increases from zero to a maximum and then decreases in a manner similar to the batch system. Unlike the controlled-power batch system, however, the entire microchannel is at steady-state, so ΔT_{ss} varies with location owing to the non-isothermal nature of the flow system. To provide an analogy to the batch system for analytical model validation in a later section, we define ΔT_{ss}^{*} to be the ΔT_{ss} at which $dT/dz = 0$, where a steady state in temperature is achieved and the MW power dissipation matches the heat losses to the environment. For the present system and conditions, ΔT_{ss} ranges from 0 to a ΔT_{max} of 17.0 °C, while ΔT_{ss}^{*} is 1.5 °C.

The alignment of ΔT_{max} with the fastest-heating zone of the microchannel prompts a comparison of ΔT_{ss} and power dissipation. With calorimetric assumptions, we use dT/dz (derived from a polynomial fit of temperature), the superficial velocity, and the heat capacity to calculate calorimetric power dissipation. As shown in Figure 6b, ΔT_{ss} and power dissipation are intimately connected, indicating a strong influence of the power dissipation on the temperature difference – an effect observed in the batch system as well.

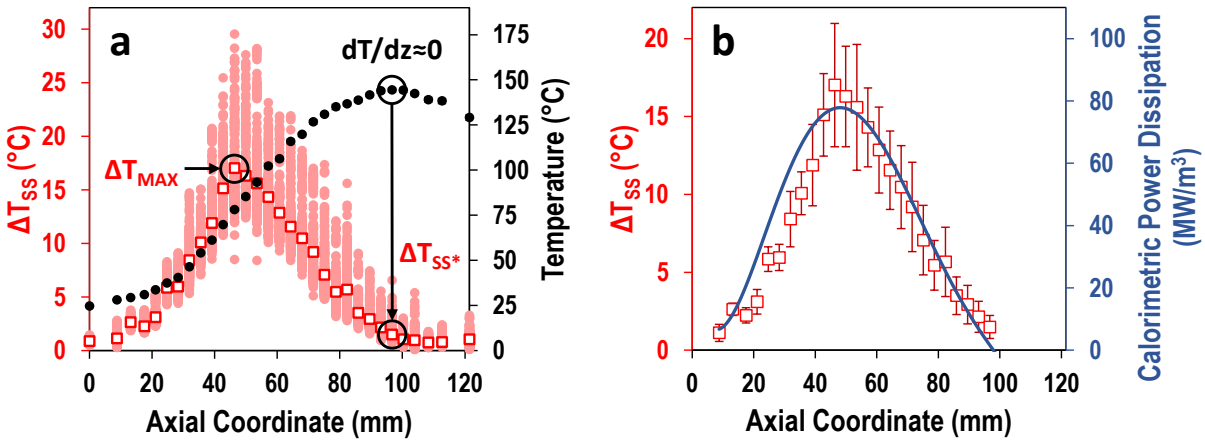

Figure 6. Axial temperature and distribution of temperature difference between phases in a 0.063" ID microchannel (a). Black circles indicate average system temperature, rose circles the full distribution of ΔT_{ss}, and red/white squares ΔT_{ss} averages. Comparison of axial power dissipation and averaged ΔT_{ss} (b). Red/white squares indicate ΔT_{ss} averages and the blue line indicates the power dissipation as derived from a polynomial fit of the temperature. Error bars indicate the

standard deviation of ΔT_{ss} for each axial coordinate. Averaged values in all cases are taken from a 1-minute sampling period after the system had achieved steady-state.

We further investigate temperature differences in MW-heated flow systems by testing microchannels of various diameters. We have chosen a flowrate for each diameter to provide an equal heat transfer coefficient, calculated by assuming the organic phase flows through aqueous spheres (slugs).[59] In Table 2, each set of conditions is summarized and accompanied by calculated and measured quantities. Axial temperature profiles, heat transfer coefficients, and power dissipation calculations are available in the SI. The specific surface area is calculated assuming that slugs are oblate spheroids in shape, with two of the three axes defined by the tubing diameter and the third by the slug length. The listed maximum power dissipation (Q_{max}) is calculated calorimetrically as in Figure 6b.

Table 2. Flow conditions and resultant observations.

Flow Condition:		**A**	**B**	**C**	**D**
Inner Diameter	*(inch)*	0.030	0.040	0.063	0.093
Total Flowrate	*(mL/min)*	0.038	0.165	1.000	4.000
Superficial Velocity	*(mm/s)*	1.39	3.39	8.42	15.21
Heat Transfer Coefficient	*(W/m^2K)*	500	500	500	500
Observed Length	*(mm)*	5.49	2.34	0.99	3.59
Specific Surface Area	*(m^2/m^3)*	6228	4955	4932	3075
Applied MW Power	*(W)*	40	40	80	120
Max Power Dissipation	*(MW/m^3)*	26.5	39.7	78.6	149.4
ΔT_{MAX}	*(°C)*	2.4	11.0	17.0	36.8
ΔT_{SS}^*	*(°C)*	1.2	4.0	1.5	5.5

As shown in Figure 7a, Q_{max} correlates positively with ΔT_{max}. For similar overall temperature profiles at each flow condition, the increases in superficial velocity and applied MW power enhance the MW power absorption and the temperature difference. This effect is profound,

with ΔT_{max} as large as 36.8 °C in our experiments. While ΔT_{ss}^{*} is much smaller than ΔT_{max} for these flow systems, they generally scale with ΔT_{max} and can be tuned. Figure 7b demonstrates the impact of flowrate ratio for two sets of tubing diameters. For each tube diameter, decreasing the ratio of the aqueous phase to the organic phase increases ΔT_{ss}. This effect, also observed in the batch system, is most pronounce for the larger tubings. Together, Figure 7a and Figure 7b demonstrate many approaches that can tune the temperature difference in continuous flow systems.

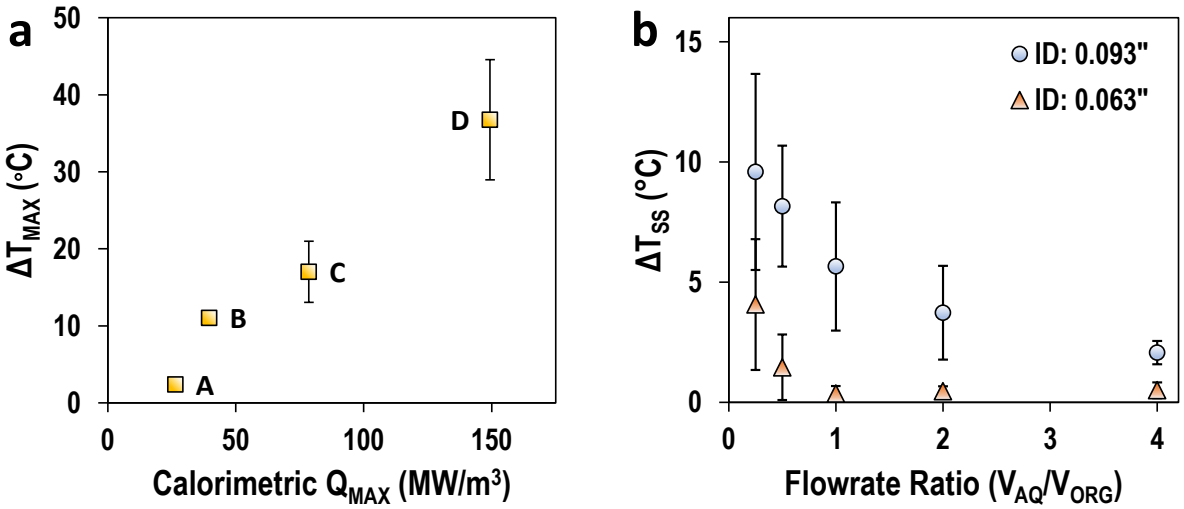

Figure 7. Influence of power dissipation on ΔT for four flow cases indicated with the data callouts (a). Effect of flow rate ratio on ΔT (b). Error bars are the standard deviation of the ΔT distribution.

Analytical model for a biphasic system

To further delineate the biphasic behavior and understand the development of temperature difference between phases in batch and flow systems, a simple analytical model is developed, using an approach inspired by a recently developed analytical model for temperature difference between the dispersed particles and liquid in a slurry under MW heating[17]. Assuming uniform mixing in each phase and neglecting the heat losses to the surrounding[17], we can write the overall energy conservation equations for each phase as

$$\rho_a C_{p,a} V_a \frac{dT_a}{dt} = Q_a V_a - UA(T_a - T_o) \tag{6}$$

$$\rho_o C_{p,o} V_o \frac{dT_o}{dt} = Q_o V_o + UA(T_a - T_o) \tag{7}$$

where ρ is the density, C_p is the specific heat capacity, V denotes the volume, T represents the temperature, Q is the dissipated power, U is the overall heat transfer coefficient between phases, and A is the interfacial area between phases. The subscripts a and o denote aqueous and organic phases, respectively. For commonly used organic solvents, we assume $\rho = \rho_a \sim \rho_o$ and $C_p = C_{p,a} \sim 2C_{p,o}$. Here, $\phi = V_a/V_o$ denotes the aqueous-to organic volume ratio, $\Delta Q =$

$Q_a - Q_o$ represents the power dissipation density difference between two phases, and $\Delta T = T_a - T_o$ is the temperature difference between phases. By subtracting the two equations, we obtain

$$\frac{d(\Delta T)}{dt} = \frac{\Delta Q}{\rho C_p} - \frac{UA\Delta T}{\rho C_p}\left(\frac{1}{V_a} + \frac{2}{V_o}\right) = \frac{\Delta Q}{\rho C_p} - \frac{UA\Delta T}{\rho C_p V_a}(1 + 2\phi) \tag{8}$$

Assuming that Q_a remains constant with time, Eq. (8) can be integrated to obtain the temperature difference

$$\Delta T = \Delta T_{ss}(1 - e^{-\frac{t}{\tau}}) \tag{9}$$

$$\Delta T_{ss} = \frac{\Delta Q}{U \cdot SSA \cdot (1+2\phi)} \tag{10}$$

$$\tau = \frac{\rho C_p}{U \cdot SSA \cdot (1+2\phi)} \tag{11}$$

Here ΔT_{ss} is the steady-state temperature difference; τ is the time scale associated with the increase in the temperature difference between the two phases; and $SSA = A/V_a$ represents the specific surface area of the aqueous phase. Eq. (9) shows that ΔT varies exponentially with a characteristic time scale τ. Both ΔT_{ss} and τ increase when decreasing the overall heat transfer coefficient, specific surface area, or aqueous-to-organic volume ratio. When the heat transfer coefficient and the specific surface area decrease, the rate of energy transferred from the aqueous to the organic phase decreases, leading to a larger ΔT_{ss} and τ. Moreover, when the aqueous-to-organic volume ratio decreases, the energy needed for heating the organic phase increases, leading to a larger ΔT. ΔT_{ss} is positively correlated to the dissipated power difference between phases. Generally, the low dielectric-loss organic solvent absorbs a small amount of power. In this regard, we assume $Q_o \sim 0$ and $\Delta Q \sim Q_a$ for most cases, indicating the ΔT_{ss} is positively affected by the power dissipated into the aqueous phase. Moreover, we can tune the ΔT_{ss} by simply increasing the input power to increase the power dissipation. This is consistent with the positive correlation we observed in both batch and flow systems. In this regard, one can use Eq. (10) to select the proper materials and parameters to tune ΔT_{ss}. Then, given an initial temperature T_i, the temperature evolution of both aqueous and organic phases T_a and T_o can be derived using Eq. (9) with Eq. (6) and Eq. (7), as shown in Eq. (12) and (13),

$$T_a = T_i + \Delta T_{ss}\left(\frac{2\phi}{1+2\phi}\frac{t}{\tau} + \frac{1}{1+2\phi}(1 - e^{-\frac{t}{\tau}})\right) \tag{12}$$

$$T_o = T_i + \frac{2\phi}{1+2\phi}\Delta T_{ss}\left(\frac{t}{\tau} - (1 - e^{-\frac{t}{\tau}})\right) \tag{13}$$

One can estimate the ΔT_{ss} and T_o using Eqs. (10) and (13) and simply measure the aqueous phase temperature since τ is independent of the dissipated power. τ depends on the material properties and reaction conditions, all known parameters, and the heat transfer coefficient, which can be estimated for each system using a suitable empirical correlation. This analytical model provides an easy way to infer the temperature difference between phases.

To assess the model, Figure 8a compares the predicted ΔT_{ss} at various conditions for flow and batch systems discussed above. Specific surface areas of batch systems are defined as the interface between two phases divided by the volume of the water, while those of the flow system are described in Table 2. The heat transfer coefficient U for the batch system is estimated using the Chilton, Drew, and Jebens correlation.[60] For the flow system, we assume the organic phase flows through aqueous spheres (slugs).[59] The overall heat transfer coefficients are 9000 W/m^{2}K and 500 W/m^{2}K for the batch and flow systems, respectively. The former is much higher because of the laboratory reactor's stirring rate (900 rpm). In Figure 8a, the red-colored area depicts the analytical model for a range of power dissipation values (Q_a = 10–25 MW/m^3) observed in COMSOL for the batch system at steady-state, while the batch experimental data is overlaid. For the flow system, COMSOL simulations were not performed due to the computational cost, making Q_a difficult to quantify. As a rough estimate, the power dissipation in batch mode (Q_a = 10–25 MW/m^3) is used in flow mode, but limited to the locations where the MW power dissipation briefly matches heat losses to the environment (i.e., where ΔT_{ss}^* is located). The predicted ΔT_{ss} (or ΔT_{ss}^*) generally agrees well with the experiments for batch and flow systems. Figure 8b demonstrates the analytical model's ability to predict ΔT when Q_a is not constant. For these calculations, Eq. (8) is integrated using the regressed power profiles for each flow condition (as demonstrated in Figure 6b). The parity between model and experiment is good, indicating the model's ability to predict ΔT at steady-state and dynamic conditions.

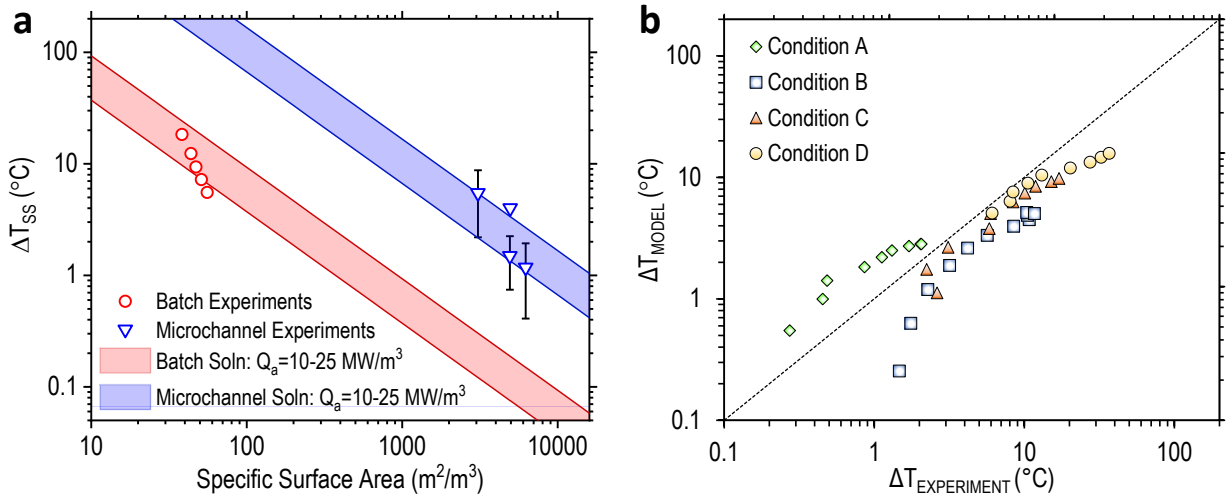

Figure 8. (a) Comparison of experimental and modeled ΔT_{ss} in batch and microfluidic systems vs. specific surface area (see text). Error bars represent triplicate experiments for batch data and the temperature distribution for flow data. (b) Demonstration of parity between experiments and model for ΔT throughout axial coordinate of microfluidic systems. Only axial coordinates up to ΔT_{max} are used for each condition to reduce the error of the calorimetric heat dissipation assumption. Error bars not plotted.

Moreover, in Figure 8a, the ΔT_{ss} of the microflow systems is lower than the batch systems at experimental conditions. Even though heat transfer is slower in the microchannel compared to the rapidly mixed batch, its ultrahigh specific surface area leads to lower ΔT_{ss} than in batch – indicating that surface area and heat transfer are vital parameters for tuning ΔT_{ss}. Based on this, we conduct a parametric analysis in a reasonable range of specific surface area (10^3–10^4 [m^2/m^3]) and heat transfer coefficient (10^2–10^3 [$W/m^2/K$]) for the flow system. Figure 9 shows that ΔT_{ss} can reach ~35 °C when the specific surface area and the heat transfer coefficient are low. There is only a narrow operating window where ΔT_{ss} is >10 °C, while the ΔT_{ss} is lower than 5 °C for most conditions. This demonstrates that, by tuning the system, one can reach a large ΔT_{max} in a very short unsteady time and a large steady state temperature ΔT_{ss}. Proper reactor types, sizes, and operating conditions can be selected to reach desired temperature difference using the analytical model.

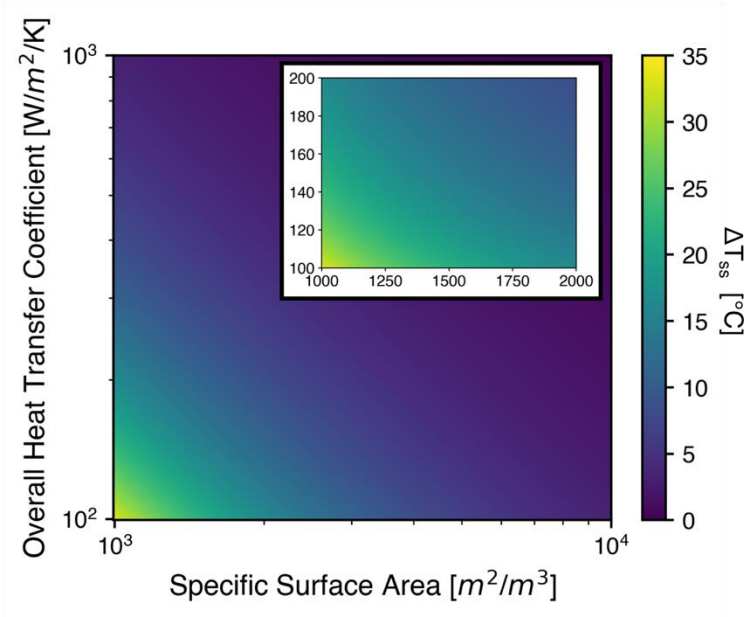

Figure 9. Analytical model-based predicted effect of the overall heat transfer coefficient and specific surface area on the temperature difference. The inset zooms in the lower-left corner, where large temperature gradients form.

Conclusions

Microwave-heated biphasic systems were studied using experiments and multiphysics COMSOL simulations to delineate the temperature gradients in such systems due to the inability of the organic solvent to absorb microwaves (true for most solvents) and the slow heat transfer from one phase to the other. Two attenuator rigs were fabricated to precisely measure and control temperature and the temperature difference, ΔT, between liquid phases for batch and flow systems. ΔT is affected by the input power, dielectric properties of the solvents, solvent volume, and the volume ratio between phases. Moreover, ΔT increases when the aqueous-to-organic volume ratio decreases at fixed volume or the aqueous volume increases at fixed volume ratio.

Similar effects are realized in continuous microflows, where the steady-state temperature difference, ΔT_{ss}, varies with location and is smaller than batch laboratory systems because of the larger specific surface area. In the temperature-ramping sections of the microflow system, where the microwave intensity is highest, ΔT is quite large, indicating intense heating and non-isothermal flow increase ΔT. A simple analytical model was developed and compared with the batch and flow experimental systems. The energy dissipation rate, heat transfer coefficient, volume ratio, and specific surface area between the phases strongly influence the temperature difference, reaching ~35 °C by proper design. This analytical model provides insights into achieving a desired steady ΔT in MW-assisted liquid-liquid separations. In a forthcoming communication, we will evaluate the impact of temperature gradients on separations and reactor performance.

Conflicts of interest

There are no conflicts to declare.

Acknowledgements

Funding from the RAPID manufacturing institute, supported by the Department of Energy (DOE) Advanced Manufacturing Office (AMO), award numbers DE-EE0007888-7.6 is gratefully acknowledged. RAPID projects at the University of Delaware are also made possible in part by funding provided by the State of Delaware. The Delaware Energy Institute gratefully acknowledges the support and partnership of the State of Delaware in furthering the essential scientific research being conducted through the RAPID projects.

References

(1) Stankiewicz, A. I.; Nigar, H. Beyond Electrolysis: Old Challenges and New Concepts of Electricity-Driven Chemical Reactors. *React. Chem. Eng.* **2020**, *5*, 1005–1016.

(2) Sebastian T. Wismann, Jakob S. Engbæk, Søren B. Vendelbo, Flemming B. Bendixen, Winnie L. Eriksen, Kim Aasberg-Petersen, Cathrine Frandsen, Ib Chorkendorff, P. M. M. Electrified Methane Reforming: A Compact Approach to Greener Industrial Hydrogen Production. *Science (80-.).* **2019**, *364*, 756–759.

(3) Ramirez, A.; Hueso, J. L.; Abian, M.; Alzueta, M. U.; Mallada, R.; Santamaria, J. Escaping Undesired Gas-Phase Chemistry: Microwave-Driven Selectivity Enhancement in Heterogeneous Catalytic Reactors. *Sci. Adv.* **2019**, *5*, eaau9000.

(4) van Geem, K. M.; Galvita, V. V.; Marin, G. B. Making Chemicals with Electricity. *Science (80-.).* **2019**, *364*, 734–735.

(5) Goyal, H.; Chen, T.-Y.; Chen, W.; Vlachos, D. G. A Review of Microwave-Assisted Process Intensified Multiphase Reactors. *Chem. Eng. J.* **2022**, *430*, 133183.

(6) Dimitrakis, G. A.; George, M.; Poliakoff, M.; Harrison, I.; Robinson, J.; Kingman, S.; Lester, E.; Gregory, A. P.; Lees, K. A System for Traceable Measurement of the Microwave Complex Permittivity of Liquids at High Pressures and Temperatures. *Meas. Sci. Technol.* **2009**, *20*, 045901.

(7) Gao, X.; Liu, X.; Yan, P.; Li, X.; Li, H. Numerical Analysis and Optimization of the Microwave Inductive Heating Performance of Water Film. *Int. J. Heat Mass Transf.* **2019**, *139*, 17–30.

(8) Kappe, C. O. Unraveling the Mysteries of Microwave Chemistry Using Silicon Carbide Reactor Technology. *Acc. Chem. Res.* **2013**, *46*, 1579–1587.

(9) Kappe, C. O.; Pieber, B.; Dallinger, D. Microwave Effects in Organic Synthesis: Myth or Reality? *Angew. Chemie - Int. Ed.* **2013**, *52*, 1088–1094.

(10) Li, H.; Liu, J.; Li, X.; Gao, X. Microwave-Induced Polar/Nonpolar Mixture Separation Performance in a Film Evaporation Process. *AIChE J.* **2019**, *65*, 745–754.

(11) Motasemi, F.; Afzal, M. T. A Review on the Microwave-Assisted Pyrolysis Technique. *Renew. Sustain. Energy Rev.* **2013**, *28*, 317–330.

(12) Zhao, Z.; Shen, X.; Li, H.; Liu, K.; Wu, H.; Li, X.; Gao, X. Watching Microwave-Induced Microscopic Hot Spots via the Thermosensitive Fluorescence of Europium/Terbium Mixed-Metal Organic Complexes. *Angew. Chemie Int. Ed.* **2021**, *300350*, 1–8.

(13) Horikoshi, S.; Kamata, M.; Serpone, N. Energy Savings through Microwave Selective Heating of Pd/AC Catalyst Particulates in a Fixed-Bed Reactor. *Chem. Eng. Technol.* **2016**, *39*, 1575–1577.

(14) Horikoshi, S.; Kamata, M.; Sumi, T.; Serpone, N. Selective Heating of Pd/AC Catalyst in Heterogeneous Systems for the Microwave-Assisted Continuous Hydrogen Evolution from Organic Hydrides: Temperature Distribution in the Fixed-Bed Reactor. *Int. J. Hydrogen Energy* **2016**, *41*, 12029–12037.

(15) Julian, I.; Pedersen, C. M.; Achkasov, K.; Hueso, J. L.; Hellstern, H. L.; Silva, H.; Mallada, R.; Davis, Z. J.; Santamaria, J. Overcoming Stability Problems in Microwave-Assisted Heterogeneous Catalytic Processes Affected by Catalyst Coking. *Catalysts* **2019**, *9*, 1–14.

(16) Julian, I.; Pedersen, C. M.; Jensen, A. B.; Baden, A. K.; Hueso, J. L.; Friderichsen, A. V.; Birkedal, H.; Mallada, R.; Santamaria, J. From Bench Scale to Pilot Plant: A 150x Scaled-up Configuration of a Microwave-Driven Structured Reactor for Methane Dehydroaromatization. *Catal. Today* **2022**, *383*, 21–30.

(17) Goyal, H.; Sadula, S.; Vlachos, D. G. Microwave Heating of Slurries. *Chem. Eng. J.* **2021**, *417*, 127892.

(18) Julian, I.; Ramirez, H.; Hueso, J. L.; Mallada, R.; Santamaria, J. Non-Oxidative Methane Conversion in Microwave-Assisted Structured Reactors. *Chem. Eng. J.* **2019**, *377*, 119764.

(19) Malhotra, A.; Chen, W.; Goyal, H.; Plaza-Gonzalez, P. J.; Julian, I.; Catala-Civera, J. M.; Vlachos, D. G. Temperature Homogeneity under Selective and Localized Microwave Heating in Structured Flow Reactors. *Ind. Eng. Chem. Res.* **2021**, *60*, 6835–6847.

(20) Ramirez, A.; Hueso, J. L.; Mallada, R.; Santamaria, J. Microwave-Activated Structured Reactors to Maximize Propylene Selectivity in the Oxidative Dehydrogenation of Propane. *Chem. Eng. J.* **2020**, *393*, 124746.

(21) Chen, W.; Malhotra, A.; Yu, K.; Zheng, W.; Plaza-Gonzalez, P. J.; Catala-Civera, J. M.; Santamaria, J.; Vlachos, D. G. Intensified Microwave-Assisted Heterogeneous Catalytic Reactors for Sustainable Chemical Manufacturing. *Chem. Eng. J.* **2021**, *420*, 130476.

(22) Li, H.; Zhao, Z.; Xiouras, C.; Stefanidis, G. D.; Li, X.; Gao, X. Fundamentals and Applications of Microwave Heating to Chemicals Separation Processes. *Renew. Sustain. Energy Rev.* **2019**, *114*, 109316.

(23) Werth, K.; Lutze, P.; Kiss, A. A.; Stankiewicz, A. I.; Stefanidis, G. D.; Górak, A. A Systematic Investigation of Microwave-Assisted Reactive Distillation: Influence of Microwaves on Separation and Reaction. *Chem. Eng. Process. Process Intensif.* **2015**, *93*, 87–97.

(24) Li, H.; Meng, Y.; Shu, D.; Zhao, Z.; Yang, Y.; Zhang, J.; Li, X.; Fan, X.; Gao, X. Breaking the Equilibrium at the Interface: Microwave-Assisted Reactive Distillation (MARD). *React. Chem. Eng.* **2019**, *4*, 688–694.

(25) Stefanidis, G. D.; Muñoz, A. N.; Sturm, G. S. J.; Stankiewicz, A. A Helicopter View of Microwave Application to Chemical Processes: Reactions, Separations, and Equipment Concepts. *Rev. Chem. Eng.* **2014**, *30*, 233–259.

(26) Liu, K.; Zhao, Z.; Li, H.; Li, X.; Gao, X. Development of a Novel MW-VLE Model for Calculation of Vapor–Liquid Equilibrium under Microwave Irradiation. *Chem. Eng. Sci.* **2022**, *249*, 117354.

(27) Zhao, Z.; Li, H.; Sun, G.; Tang, X.; Wu, H.; Gao, X. Predicting Microwave-Induced Relative Volatility Changes in Binary Mixtures Using a Novel Dimensionless Number. *Chem. Eng. Sci.* **2021**, *237*.

(28) Hiranvarachat, B.; Devahastin, S. Enhancement of Microwave-Assisted Extraction via Intermittent Radiation: Extraction of Carotenoids from Carrot Peels. *J. Food Eng.* **2014**, *126*, 17–26.

(29) Papoutsis, K.; Pristijono, P.; Golding, J. B.; Stathopoulos, C. E.; Bowyer, M. C.; Scarlett, C. J.; Vuong, Q. V. Enhancement of the Total Phenolic Compounds and Antioxidant Activity of Aqueous Citrus Limon L. Pomace Extract Using Microwave Pretreatment on the Dry Powder. *J. Food Process. Preserv.* **2017**, *41*, e13152.

(30) Badwaik, L. S.; Borah, P. K.; Deka, S. C. Optimization of Microwave Assisted Extraction of Antioxidant Extract from Garcinia Pedunculata Robx. *Sep. Sci. Technol.* **2015**, *50*, 1814–1822.

(31) Nikousaleh, A.; Prakash, J. Antioxidant Components and Properties of Dry Heat Treated Clove in Different Extraction Solvents. *J. Food Sci. Technol.* **2016**, *53*, 1993–2000.

(32) Ranic, M.; Nikolic, M.; Pavlovic, M.; Buntic, A.; Siler-Marinkovic, S.; Dimitrijevic-Brankovic, S. Optimization of Microwave-Assisted Extraction of Natural Antioxidants from Spent Espresso Coffee Grounds by Response Surface Methodology. *J. Clean. Prod.* **2014**, *80*, 69–79.

(33) Gao, X.; Li, X.; Zhang, J.; Sun, J.; Li, H. Influence of a Microwave Irradiation Field on Vapor-Liquid Equilibrium. *Chem. Eng. Sci.* **2013**, *90*, 213–220.

(34) Breeden, S. W.; Clark, J. H.; Farmer, T. J.; MacQuarrie, D. J.; Meimoun, J. S.; Nonne, Y.; Reid, J. E. S. J. Microwave Heating for Rapid Conversion of Sugars and Polysaccharides to 5-Chloromethyl Furfural. *Green Chem.* **2013**, *15*, 72–75.

(35) Yang, T.; Zhou, Y. H.; Zhu, S. Z.; Pan, H.; Huang, Y. B. Insight into Aluminum Sulfate-Catalyzed Xylan Conversion into Furfural in a Γ-Valerolactone/Water Biphasic Solvent under Microwave Conditions. *ChemSusChem* **2017**, *10*, 4066–4079.

(36) Ricciardi, L.; Verboom, W.; Lange, J. P.; Huskens, J. Reactive Extraction Enhanced by Synergic Microwave Heating: Furfural Yield Boost in Biphasic Systems. *ChemSusChem* **2020**, *13*, 3589–3593.

(37) Wrigstedt, P.; Keskiväli, J.; Repo, T. Microwave-Enhanced Aqueous Biphasic Dehydration of Carbohydrates to 5-Hydroxymethylfurfural. *RSC Adv.* **2016**, *6*, 18973–18979.

(38) Kappe, C. O. How to Measure Reaction Temperature in Microwave-Heated Transformations. *Chem. Soc. Rev.* **2013**, *42*, 4977–4990.

(39) Sturm, G. S. J.; Verweij, M. D.; Stankiewicz, A. I.; Stefanidis, G. D. Microwaves and Microreactors: Design Challenges and Remedies. *Chem. Eng. J.* **2014**, *243*, 147–158.

(40) Sturm, G. S. J.; Verweij, M. D.; Van Gerven, T.; Stankiewicz, A. I.; Stefanidis, G. D. On the Effect of Resonant Microwave Fields on Temperature Distribution in Time and Space. *Int. J. Heat Mass Transf.* **2012**, *55*, 3800–3811.

(41) Goyal, H.; Mehdad, A.; Lobo, R. F.; Stefanidis, G. D.; Vlachos, D. G. Scaleup of a Single-Mode Microwave Reactor. *Ind. Eng. Chem. Res.* **2020**, *59*, 2516–2523.

(42) Robinson, J.; Kingman, S.; Irvine, D.; Licence, P.; Smith, A.; Dimitrakis, G.; Obermayer, D.; Kappe, C. O. Electromagnetic Simulations of Microwave Heating Experiments Using Reaction Vessels Made out of Silicon Carbide. *Phys. Chem. Chem. Phys.* **2010**, *12*, 10793–10800.

(43) Ayappa, K. G.; Brandon, S.; Derby, J. J.; Davis, H. T.; Davis, E. A. Microwave Driven Convection in a Square Cavity. *AIChE J.* **1994**, *40*, 1268–1272.

(44) Chatterjee, S.; Basak, T.; Das, S. K. Microwave Driven Convection in a Rotating Cylindrical Cavity: A Numerical Study. *J. Food Eng.* **2007**, *79*, 1269–1279.

(45) Ratanadecho, P.; Aoki, K.; Akahori, M. A Numerical and Experimental Investigation of the Modeling of Microwave Heating for Liquid Layers Using a Rectangular Wave Guide

(Effects of Natural Convection and Dielectric Properties). *Appl. Math. Model.* **2002**, *26*, 449–472.

(46) Zhu, J.; Kuznetsov, A. V.; Sandeep, K. P. Mathematical Modeling of Continuous Flow Microwave Heating of Liquids (Effects of Dielectric Properties and Design Parameters). *Int. J. Therm. Sci.* **2007**, *46*, 328–341.

(47) Klinbun, W.; Rattanadecho, P. Analysis of Microwave Induced Natural Convection in a Single Mode Cavity (Influence of Sample Volume, Placement, and Microwave Power Level). *Appl. Math. Model.* **2012**, *36*, 813–828.

(48) Goyal, H.; Vlachos, D. G. Multiscale Modeling of Microwave-Heated Multiphase Systems. *Chem. Eng. J.* **2020**, *397*, 125262.

(49) Chen, T.-Y.; Baker-Fales, M.; Vlachos, D. G. Operation and Optimization of Microwave-Heated Continuous-Flow Microfluidics. *Ind. Eng. Chem. Res.* **2020**, *59*, 10418–10427.

(50) Ayappa, K. G.; Davis, H. T.; Crapiste, G.; Davis, E. A.; Gordon, J. Microwave Heating: An Evaluation of Power Formulations. *Chem. Eng. Sci.* **1991**, *46*, 1005–1016.

(51) Chandrasekaran, S.; Ramanathan, S.; Basak, T. Microwave Material Processing—a Review. *AIChE J.* **2012**, *58*, 330–363.

(52) Damilos, S.; Radhakrishnan, A. N. P.; Dimitrakis, G.; Tang, J.; Gavriilidis, A. Experimental and Computational Investigation of Heat Transfer in a Microwave-Assisted Flow System. *Chem. Eng. Process. - Process Intensif.* **2019**, *142*, 107537.

(53) Sturm, G. S. J.; Verweij, M. D.; Gerven, T. Van; Stankiewicz, A. I.; Stefanidis, G. D. On the Parametric Sensitivity of Heat Generation by Resonant Microwave Fields in Process Fluids. *Int. J. Heat Mass Transf.* **2013**, *57*, 375–388.

(54) Robinson, J.; Kingman, S.; Irvine, D.; Licence, P.; Smith, A.; Dimitrakis, G.; Obermayer, D.; Kappe, C. O. Understanding Microwave Heating Effects in Single Mode Type Cavities - Theory and Experiment. *Phys. Chem. Chem. Phys.* **2010**, *12*, 4750–4758.

(55) Desir, P.; Chen, T. Y.; Bracconi, M.; Saha, B.; Maestri, M.; Vlachos, D. G. Experiments and Computations of Microfluidic Liquid-Liquid Flow Patterns. *React. Chem. Eng.* **2020**, *5*, 39–50.

(56) Chen, T. Y.; Desir, P.; Bracconi, M.; Saha, B.; Maestri, M.; Vlachos, D. G. Liquid-Liquid Microfluidic Flows for Ultrafast 5-Hydroxymethyl Furfural Extraction. *Ind. Eng. Chem. Res.* **2021**, *60*, 3723–3735.

(57) Wang, K.; Li, L.; Xie, P.; Luo, G. Liquid–Liquid Microflow Reaction Engineering. *React. Chem. Eng.* **2017**, (2) No. 2, 611–627.

(58) Zhao, C. X.; Middelberg, A. P. J. Two-Phase Microfluidic Flows. *Chem. Eng. Sci.* **2011**, *66*, 1394–1411.

(59) Whitaker, S. *Fundamental Principles of Heat Transfer*; Pergamon Press, 2013.

(60) Chilton, T. H.; Drew, T. B.; Jebens, R. H. Heat Transfer Coefficients in Agitated Vessels. *Ind. Eng. Chem.* **1944**, *36*, 510–516.